MIT Open Access Articles

Spectroscopic characterization of isomerization transition states

Spectroscopic characterization of isomerization transition states

Joshua H. Baraban,[1,2] P. Bryan Changala,[1,3] Georg C. Mellau,[4]
John F. Stanton,[5] Anthony J. Merer,[6,7] Robert W. Field[1*]

[1]Department of Chemistry, Massachusetts Institute of Technology,
Cambridge, MA 02139, USA
[2]Current address: Department of Chemistry and Biochemistry,
University of Colorado, Boulder, CO 80309, USA
[3]Current address: JILA, National Institute of Standards and Technology
and Department of Physics,
University of Colorado, Boulder, CO 80309, USA
[4]Physikalisch-Chemisches Institut, Justus-Liebig-Universität Giessen,
Heinrich-Buff-Ring 58, D-35392 Giessen, Germany
[5]Department of Chemistry and Biochemistry, University of Texas at Austin
Austin, TX 78712, USA
[6]Department of Chemistry, University of British Columbia
Vancouver, B.C., Canada V6T 1Z1
[7]Institute of Atomic and Molecular Sciences, Academia Sinica
Taipei 10617, Taiwan

[*]To whom correspondence should be addressed; E-mail: rwfield@mit.edu.

**Transition state theory is central to our understanding of chemical reaction
dynamics. We demonstrate here a method for extracting transition state energies and properties from a characteristic pattern found in frequency domain
spectra of isomerizing systems. This pattern, a dip in the spacings of certain**

barrier-proximal vibrational levels, can be understood using the concept of effective frequency, ω^{eff}. The method is applied to the *cis-trans* conformational change in the S_1 state of C_2H_2 and the bond-breaking HCN-HNC isomerization. In both cases, the barrier heights derived from spectroscopic data agree extremely well with previous *ab initio* calculations. We also show that it is possible to distinguish between vibrational modes that are actively involved in the isomerization process and those that are passive bystanders.

The central concept of the transition state in chemical kinetics is familiar to all students of chemistry. Since its inception by Arrhenius (*1*) and later development into a full theory by Eyring, Wigner, Polanyi, and Evans (*2–5*), the idea that the thermal rate depends primarily on the highest point along the lowest energy path from reactants to products has remained essentially unchanged. Most of chemical dynamics is now firmly based on this idea of the transition state, notwithstanding the emergence of unconventional reactions such as roaming (*6, 7*), where a photodissociated atom wanders before abstracting from the parent fragment. Despite the clear importance of the transition state to the field of chemistry, direct experimental studies of the transition state and its properties are scarce (*8*).

Here we report the observation of a vibrational pattern, a dip in the trend of quantum level spacings, which occurs at the energy of the saddle point. This phenomenon is expected to provide a generally applicable and accurate method for characterizing transition states. Only a subset of vibrational states exhibit a dip; these states contain excitation along the reaction coordinate and are barrier-proximal, meaning that they are more susceptible to the effects of the isomerization barrier than other states. Experimental evidence for this concept is drawn from our studies of two prototypical systems, the HCN↔HNC isomerization and the *cis-trans* conformational change in the first electronically excited singlet state of acetylene.

2

Effective frequency and the isomerization dip   We must first describe effective frequency, ω^{eff}, the central quantity in our model for the spectroscopic signature of isomerizing systems. In a one-dimensional system, the effective frequency is the derivative of the energy with respect to the quantum number n

$$\omega^{\text{eff}}(n) = \frac{\partial E}{\partial n} = \frac{\Delta E}{\Delta n} \tag{1}$$

where ω^{eff} is evaluated discretely for quantized systems. ω^{eff} is a dynamic quantity that can change as excitation increases, unlike those quantities such as harmonic frequency, ω, or fundamental frequency, ν, often listed as molecular constants. As such, it is a very useful diagnostic of the behavior of the system.

Applications of effective frequency date back a long way. For example, the effective frequencies $\omega^{\text{eff}}(n)$ of a state of a diatomic molecule are its vibrational intervals, which decrease to zero at the dissociation limit. The sum of the effective frequencies is therefore the dissociation energy. In most cases it is not possible to observe the $\omega^{\text{eff}}(n)$ all the way to the dissociation limit, but a linear extrapolation to $\omega^{\text{eff}} = 0$ allows a very good estimate of the dissociation energy, notwithstanding nonlinearities in the trend of vibrational intervals near dissociation. This is the basis of the Birge-Sponer plot (*9*) where the area under a graph of the vibrational intervals, $\omega^{\text{eff}}(n)$, against n gives the dissociation energy. Leroy and Bernstein (*10*) have given a protocol for extrapolating the effective frequencies, which takes account of the exact long-range shape of the vibrational potential near dissociation. This procedure is found to give very accurate dissociation energies (*11*).

Effective frequencies also play a large part in our understanding of quasilinear molecules. A quasilinear molecule has a non-linear equilibrium geometry, but a comparatively small potential barrier to linearity. The pattern of the lowest vibrational levels is that of a bent molecule, but with increasing bending vibrational excitation this changes smoothly into the pattern for a linear molecule, vibrating with large amplitude. Dixon (*12*) has modeled a quasilinear potential as a

3

two-dimensional harmonic oscillator perturbed by a Gaussian hump at the linear configuration, and calculated its energy levels. These levels may be assigned vibrational (v) and angular momentum (K) quantum numbers. (*13*) If the vibrational intervals (effective frequencies) for a given K value are plotted against v, they pass through a minimum at the energy of the potential barrier, thereby allowing determination of its value. The depth of this "Dixon dip" is greatest for $K = 0$, and decreases with increasing K. The reason is that the angular momentum results in a K-dependent centrifugal barrier at the linear configuration, which the molecule must avoid.

We now illustrate the concept of effective frequency in more detail, with the four types of potential shown in Fig. 1. For the harmonic oscillator,

$$\omega^{\text{eff}} = \frac{\partial}{\partial n}\left[\omega\left(n + \frac{1}{2}\right)\right] = \omega, \tag{2a}$$

and

$$\frac{\partial \omega^{\text{eff}}}{\partial n} = 0, \tag{2b}$$

indicating that the dynamics of the system do not change as a function of energy.

For a Morse oscillator, where the potential is $V(r) = D_e[1 - e^{-ar}]^2$,

$$\omega^{\text{eff}} = \frac{\partial}{\partial n}\left[\omega\left(n + \frac{1}{2}\right) + x\left(n + \frac{1}{2}\right)^2\right] = \omega + x + 2nx, \tag{3a}$$

and

$$\frac{\partial \omega^{\text{eff}}}{\partial n} = 2x \tag{3b}$$

where x is always negative. This linear decrease of ω^{eff} with n reflects the migration of the Morse wavefunctions toward the softer outer turning point. When ω^{eff} reaches zero at the dissociation limit, it becomes clear that the Morse and harmonic oscillators display very different dynamics.

Simple expressions for ω^{eff} and $\frac{\partial \omega^{\text{eff}}}{\partial n}$ cannot be derived for the other cases in Fig. 1, but these illustrate the most important feature even more clearly: the effective frequency goes to
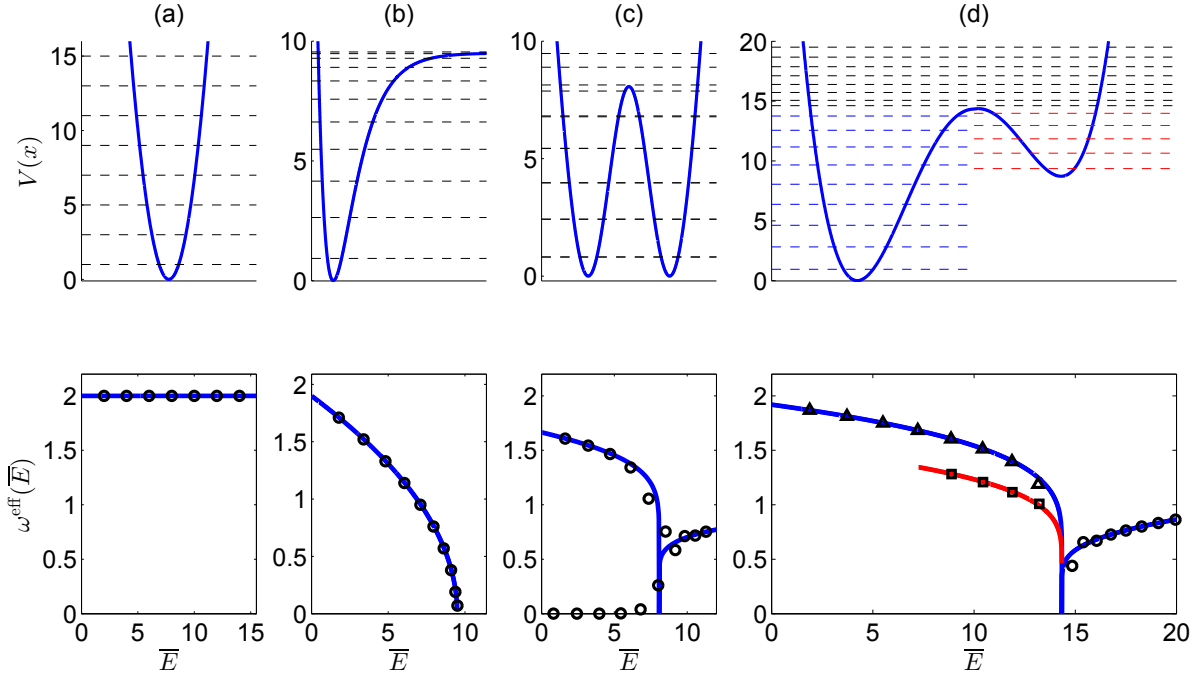
Figure 1: Effective frequency plots below their associated model potentials. From left: a) harmonic oscillator, b) Morse oscillator, c) symmetric double minimum potential, and d) asymmetric double minimum potential. In the top panels, the quantized energy levels are marked with dashed lines. In the bottom row, the classical ω^{eff} is shown as a solid line, with the quantum level spacings plotted as open circles vs. $\overline{E}$ (the mid-point energy for each interval). In (c), the upper and lower series of circles correspond to the vibrational level spacings and tunneling splittings, respectively. In (d), the ω^{eff} curve and energy levels for the second minimum are shown in red, and the quantum level spacings are overlaid on the ω^{eff} curves as triangles and squares.

zero at the energy of each stationary point on the potential. Classically, this can be understood by imagining a ball released to roll on a double minimum surface. If the ball starts on one side at exactly the height of a local maximum, it will reach that maximum with zero kinetic energy and stop. Because the ball never returns, the oscillation period is infinite and the frequency therefore is zero. We see immediately that this applies to the Morse oscillator as well – ω^{eff} reaches zero at the dissociation limit, which is a horizontal asymptote of $V(r)$. It is clear that this phenomenon is quite general and that zeros or abrupt changes in ω^{eff} signal important changes in the dynamics of the system.

In their quantum and semi-classical analysis of highly excited states of HCP, Jacobson and Child (*14*) mention a dip in ω^{eff} as the signature of an approach to a saddle point. Because the HCP↔HPC potential energy surface exhibits some unusual features (HPC is a saddle point, rather than a second minimum), and is not a true isomerization (*15*), the observed ω^{eff} trend was categorized as a peculiar "Dixon dip", rather than recognized as the universal signature proposed here. Similarly, the onset of internal rotation in the ground state of SiC_2 (*16*) is not an isomerization, though the ideas presented here are applicable to it. More generally, the behavior of systems as they encounter stationary points has been investigated from other perspectives as well (*17–20*). For our purposes, it suffices that this dip in ω^{eff} provides a marker of the chemically relevant transition state energy, as we demonstrate here with experimental data, following an explanation of the method for measuring transition state energies and a discussion of its application.

A model for measurement of the transition state energy In order to determine the transition state energy, we propose the following semi-empirical formula for ω^{eff} as a function of energy, $\overline{E}$, defined as the mid-point energy for each vibrational interval:

$$\omega^{\text{eff}}(\overline{E}) = \omega_0 \left(1 - \frac{\overline{E}}{E_{TS}} \right)^{1/m} \qquad \omega_0, E_{TS} \geq 0; \;\; 2 \leq m \leq \infty; \;\; \overline{E} \leq E_{TS} \qquad (4)$$
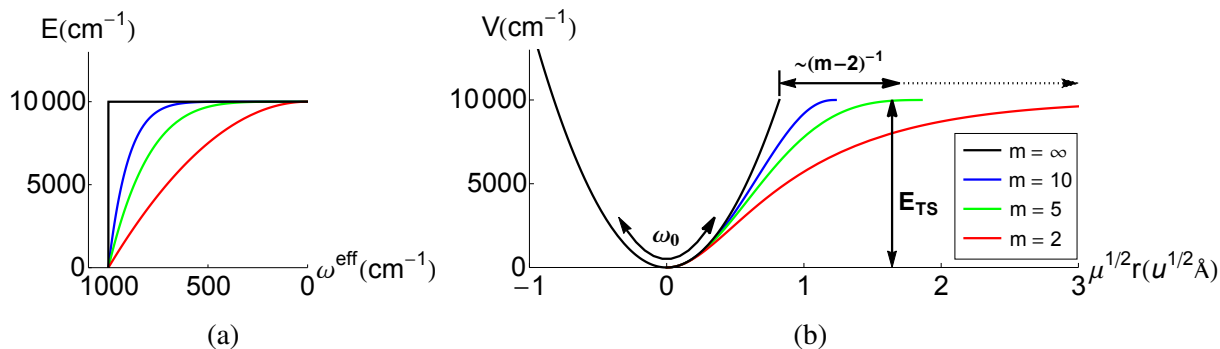
Figure 2: Relationship between potential shape and ω^{eff} illustrated by (a) effective frequency curves and (b) the corresponding potentials as a function of the shape parameter m in Eq. 4.

where ω_0 is the effective frequency at $\overline{E} = 0$ for the progression being analyzed, E_{TS} is the energy of the transition state, and m is a parameter related to the barrier shape. For the Morse oscillator (Fig. 1b), $m = 2$ analytically (*21–23*), $E_{TS} = D_e$, the dissociation energy, and $\omega_0 = \omega$, the harmonic frequency. Equation 4 can be regarded as a generalization of the Morse formula where m is allowed to take values greater than 2. The formula also satisfies the required physical boundary conditions of a limiting harmonic frequency ω_0 at $\overline{E} = 0$ and $\omega^{\text{eff}} = 0$ at $\overline{E} = E_{TS}$.

The dependence of the m parameter on potential shape is illustrated in Fig. 2 (See supplementary text for further details.). The lower limit is $m = 2$, the Morse oscillator, where the asymptote is approached infinitesimally with r. The other limit is a truncated harmonic oscillator where the potential abruptly becomes constant at E_{TS}. In such a case ω^{eff} falls instantly to zero and $m = \infty$.

Dissociation vs. isomerization The physical arguments presented here regarding the behavior of ω^{eff} vs. $\overline{E}$ (and therefore Eq. 4) pertain only up to $\overline{E} = E_{TS}$. Above that energy, ω^{eff} can either remain at zero for an unbound system (as with the Morse oscillator), or rise again (in a bound system). The above-barrier behavior of ω^{eff} depends on the outer walls of the potential,

and is not described by Eq. 4. The mth root form of Eq. 4 suggests the presence of a branch point at E_{TS}, which separates the above-barrier and below-barrier eigenspectra into two distinct energy regions (*19, 24*).

A semiclassical analysis of long-range interatomic potentials of the form $D - C/r^n$ was performed by LeRoy and Bernstein (*10*) over 40 years ago. They derived an expression that relates the change in energy per quantum number (i.e. the effective frequency) near the dissociation limit to a quantity proportional to $(1 - E/D)^{(n+2)/2n}$. This expression is clearly similar to our effective frequency formula, but the two models treat dynamically and mathematically distinct regimes. For inverse power law potentials where $n = \{1, 2, 3, 4, \ldots\}$, the corresponding m values are $\{2/3, 1, 6/5, 4/3, \ldots\}$. In the limit $n \to \infty$, the effective m value approaches 2 from below. In contrast, our model has a lower limit of $m = 2$. In other words, these two similar effective frequency expressions treat essentially disjoint classes of potentials. The key difference is how the stationary point (or dissociation limit) is approached. For long-range potentials with inverse power law forms, the stationary point at $r \to \infty$ is approached only polynomially. Our treatment considers potentials where stationary points are local maxima and therefore approached over a finite domain. The common system, the Morse potential, has a stationary point at $r \to \infty$, but approaches it exponentially (that is, faster than any power law,) and is in some sense simultaneously long-range and local. Graphically, the dynamical distinction corresponds to positive curvature (LeRoy-Bernstein) vs. negative curvature (our model) on a Birge-Sponer plot, with the linear plot of the Morse oscillator dividing the two regimes.

Practical application   It remains to discuss how best to extract the desired saddle point energy from spectroscopically measured quantities. From the frequency domain spectrum we measure the energies of a series of quantized vibrational levels, and take the average $\overline{E}$ and difference ω^{eff} of adjacent level energies to obtain a set of $(\overline{E}, \omega^{\text{eff}})$ data points (*25*). Equivalently, time

domain spectroscopy may provide alternative or more direct ways to obtain vibrational periods or frequencies vs. energy, especially for larger systems. A plot of these $(\overline{E}, \omega^{\text{eff}})$ data reveals any dynamical trend in ω^{eff}, either constant, linear, or nonlinear. If a stationary point is present within the data range of $\overline{E}$, the plot will dip to a minimum as the energy of the stationary point is approached, though in a bound quantum system there will never be a point with ω^{eff} equal to zero.

In principle, only this bare minimum of information is necessary to apply Eq. 4. A value for E_{TS} can then be obtained, which in favorable cases should have an uncertainty of 5 to 10% of the effective frequency, depending on the extent and quality of the input data. High resolution and detailed spectroscopic assignments are not a requirement, nor are *ab initio* calculations, although these can help identify the active vibrations and the nature of the transition state. Even in larger molecules, where full spectroscopic and computational analyses are impractical, the problem must simplify to a very small number of vibrational modes that form the reaction coordinate and lead to the transition state. These active vibrations reveal themselves by their isomerization dips.

In order to demonstrate the capabilities of our method, we now apply our model to two prototypical isomerizing molecules, HCN and the S_1 state of C_2H_2. These systems have been spectroscopically characterized in great detail, such that we can apply the isomerization dip method and Eq. 4 to them with confidence. We emphasize that the levels of knowledge and quality of data available for these systems are not necessary in general for the application of our method. Furthermore, despite the small sizes of HCN and C_2H_2, they exhibit many of the complications expected in larger molecules. Only brief backgrounds need be given here for these molecules, as the cited references provide full details.

The examples of S_0 HCN↔HNC and S_1 C_2H_2 The potential surface for the electronic ground state of the [H,C,N] system has two minima, the linear HCN and HNC isomers, separated by approximately 5200 cm^{-1}. The reaction coordinate of the bond-breaking HCN-HNC isomerization corresponds mainly to the ν_2 bending vibration, and the barrier to isomerization is nearly 17000 cm^{-1} above the HCN minimum. Extensive experimental term values for both isomers are available up to 10000 cm^{-1} above the HCN minimum (*26*). To continue the analysis up to and beyond the barrier energy, we used spectroscopically assigned *ab initio* eigenenergies (*26–28*). In Ref. (*26*), levels with high bending excitation were reported to deviate unexpectedly from effective Hamiltonian predictions, reflecting the presence of the double well potential.

The S_1 state of C_2H_2 supports *cis* and *trans* conformers, with the *cis* conformer lying approximately 2672 cm^{-1} above the *trans*. As illustrated in Fig. 3, the transition state is planar and nearly half-linear (*29*). The bare saddle point energy is calculated to be 4979 cm^{-1} above the *trans* minimum, but with an uncertainty of hundreds of cm^{-1}, even for the most accurate calculations to date (*30*). A torsional isomerization path might have been expected, on the basis of *cis-trans* isomerizations in other molecules, but this is not found here.

The height of the barrier compared to the fundamental frequencies leads us to expect at least some normal vibrational structure, even in the shallower *cis* well. Thus far, several *cis* vibrational levels have been identified, in reasonable agreement with *ab initio* calculations (*31–33*). In the *trans* well, almost all of the vibrational levels below the barrier have been assigned (*33*). Of the six *trans* conformer vibrational modes, four are fairly well-behaved: the Franck-Condon active vibrations ν_2 (CC stretch) and ν_3 (*trans*-bend) (*34*), and the CH stretching modes ν_1 and ν_5 (*35, 36*). On the other hand, a large portion of the *trans* vibrational manifold can only be understood within the framework of bending polyads $B^{n=(v_4+v_6)}$ (*37*), because of the Darling-Dennison and Coriolis interactions between the low frequency $ungerade$ bending modes, ν_4
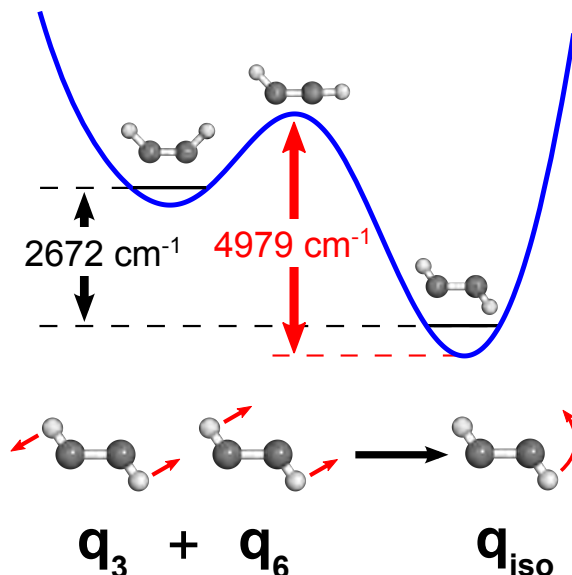
Figure 3: Salient features of the *cis-trans* isomerization in S_1 C_2H_2. The barrier height and energy difference between the two conformers are shown, as well as the combination of *trans* normal modes (q_3 and q_6) that corresponds to the isomerization coordinate.

(torsion) and ν_6 (*cis*-bend).

Despite the success of the polyad model in reproducing the level structures associated with the bending vibrations, there are disturbing exceptions. As illustrated in Fig. 13 of Ref. (*38*), the series of $3^n B^2$ polyads exhibits a surprising trend, with the energy of the lowest member of the polyad decreasing rapidly relative to the energies of the other polyad members. Although inexplicable by conventional models, this occurrence turns out to be intimately related to the isomerization dynamics discussed here.

Determination of the barrier height   We now apply the isomerization dip concept, and in particular Eq. 4, to the barrier proximal energy levels discussed in the previous section.

Figure 4 shows the results of the pure bending $\left(\omega_2^{\mathrm{eff}}\right)$ effective frequency analysis for HCN/HNC. The barrier heights for both wells are found to be within 1% of the *ab initio* values. In order to compare E_{TS} to calculated barrier heights, either the *ab initio* zero point energy must
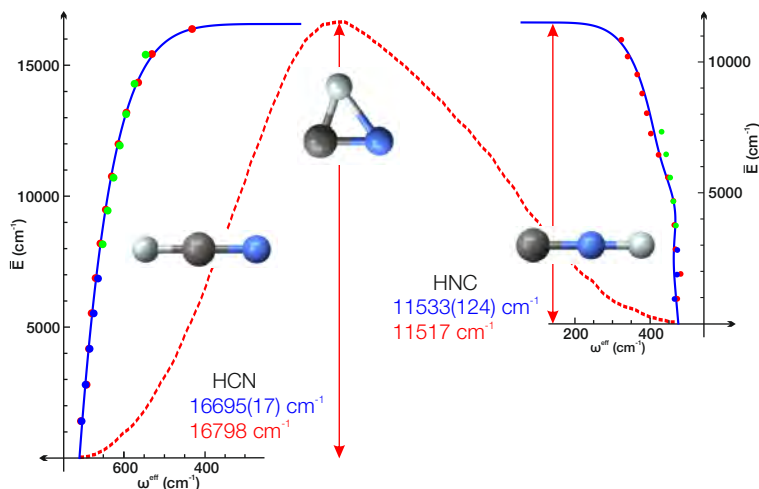
Figure 4: The ω_2^{eff} ($\ell = 0$) effective frequency analysis for HCN and HNC. Shown are experimental data points (blue), Dunham-based predictions using only experimental data (green), and the assigned *ab initio* data points (red) *(26)*. (See supplementary text for details.) The fitted E_{TS} parameters using Eq. 4 (blue) are compared with the *ab initio* barrier heights (red). A one dimensional cut through the PES is shown as a red dashed line. The unusual shapes of the HNC potential and ω^{eff} plot near 5000 cm^{-1} result from interaction with a low-lying excited diabatic electronic state *(44)*.

be subtracted from the calculated barrier height, or an effective zero point energy must be added to the fitted E_{TS} value. (See supplementary text for details.) A consistency check of the HCN/HNC analysis stems from another dynamical parameter that affects ω_2^{eff} and the effective barrier height: the vibrational angular momentum, ℓ. The fitted E_{TS} barrier heights are summarized in Table S5 and, as expected, the barrier height increases approximately quadratically with ℓ.

Figure 5a shows plots of ω_3^{eff} and ω_6^{eff} for the $3^n 6^2$ series of C_2H_2, where Eq. 4 can be seen to fit the observed data very well. (Details of the fits can be found in Tables S1 and S2.) The $3^n 6^2$ levels experience the effects of the barrier most strongly, whereas the 3^n levels are completely uninfluenced by it, because a combination of q_3 and q_6 is required to access the transition state geometry. Both ω_3^{eff} and ω_6^{eff} can be obtained as a function of v_6 as well, reading the array of term values in Table S2 horizontally rather than vertically. The same $\{\overline{E}, \omega^{\text{eff}}\}$ data are
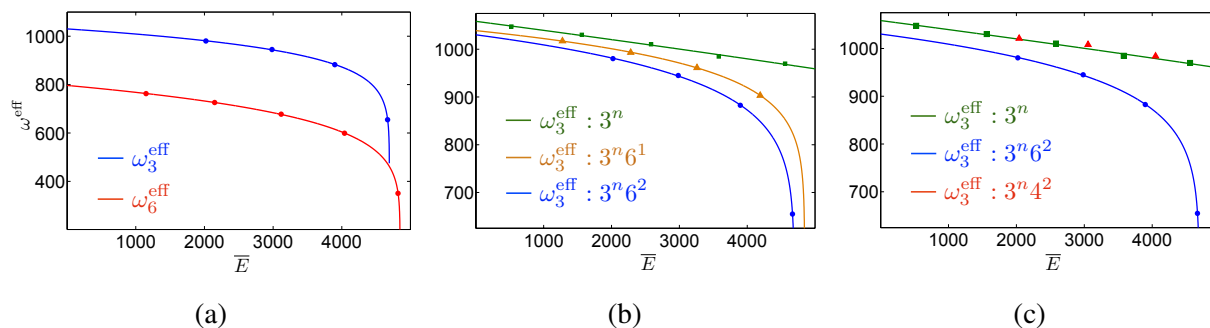
Figure 5: The ω^{eff} analysis for S_1 C_2H_2. The dip is expected near the *ab initio* value of 4979 cm^{-1}. Data from Tables S1 to S3. (a) Experimental ω^{eff} for the 3^n6^2 levels, shown with fits to Eq. 4. ω_3^{eff} is obtained directly from the progression of 3^n6^2 levels, and ω_6^{eff} is derived from the 3^n6^2 and 3^n6^1 levels at a given n_3. (b) Experimental ω_3^{eff} for the 3^n6^2 levels as compared to ω_3^{eff} for other progressions with varying quanta of ν_6, shown with fits to Eq. 4. The 3^n6^2 series has the sharpest dip, in close analogy to the $K = \ell = 0$ series in the "Dixon dip" (*12*). (c) ω_3^{eff} plots for the 3^n, 3^n4^2, and 3^n6^2 progressions. The 3^n4^2 series follows the normal behavior of the 3^n levels, despite the isomerization dip observed in the 3^n6^2 levels. This shows that the torsional mode ν_4 is not involved in the isomerization process at these energies.

obtained, but in different sets.

Reaction path analysis   Several possibilities arise when the ω^{eff} analysis is extended to additional vibrational progressions. The first, shown in Fig. 5c, is that of differentiating between isomerization pathways. We have noted already that certain progressions, such as the 3^n of *trans* C_2H_2, show no sign of an isomerization dip. Here we see that surprisingly, the 3^n4^2 levels exhibit the same ω_3^{eff} as the 3^n, from which we conclude that the torsional *cis-trans* isomerization pathway is closed at these energies. This observation is consistent with the harmonic behavior in ν_4 noted in Ref. (*37*). Furthermore, the very strong interactions between ν_4 and ν_6, as well as the inevitable evolution of the torsion as the molecule straightens, would have led us to predict some kind of nonlinear behavior of the ω_3^{eff} from the 3^n4^2 levels. The absence of any such effects implies that the torsion is a spectator mode independent of the isomerization occurring in ν_3 and ν_6. Unlike in many other molecules, torsion does not play a role in this

13

cis-trans isomerization. It appears that the residual π-bond, despite its incomplete complement of substituents, leads to the preference for in-plane isomerization. (Fig. 3).

The clear distinction between spectator modes and isomerizing modes suggests that other properties of the saddle point may be obtainable from ω^{eff} analysis. Consider a separable system that consists of an asymmetric double minimum in x, and a harmonic oscillator in y: $V(x, y) = V(x) + ky^2/2$. Because the Hamiltonian is separable, $E = E_x + E_y$, and therefore ω_x^{eff} does not depend on y, in the same way that ω_3^{eff} does not depend on v_4 in *trans* S_1 C_2H_2. This means that the ω_y of the transition state is unchanged from that of the minimum. We can then imagine a case where $\dfrac{\partial^2 V(x, y)}{\partial y^2}$ varies with x. In such a case it is possible to extract a value for ω_y of the transition state from the spacing of the ω_x^{eff} curves, or by plotting ω_y^{eff} directly, including data from above the saddle point energy. (*39*) To give a specific example from a rotational degree of freedom, a quadratic fit of the ℓ-dependence of the $0v_20$ HCN barrier height (Table S5) yields $\left(A - \overline{B}\right)_{TS} = 11.1(9)$ cm^{-1} for the transition state, which agrees well with the *ab initio* value of 12.2 cm^{-1}. These hitherto unmeasurable transition state rotational constants and frequencies, in addition to the saddle point energy, are critical inputs to the expression for the rate constant in transition state theory (*2*).

The ideas about spectator modes articulated here are confirmed by analysis of the HCN/HNC stretching mode progressions - neither shows any dip up to 19000 cm^{-1} above the HCN minimum. Furthermore, the shifts in the fitted barrier heights for v_2 progressions built upon excitation in ν_1 and ν_3 match well with the 1D pseudopotentials $V_{v_1, v_3}(\theta)$ from Ref. (*40–42*) and the stretching frequencies (Table S4).

Implications and outlook   The method described here provides qualitative and quantitative information about the isomerization mechanism and the transition state solely on the basis of experimental data. The reaction coordinate can be identified from the isomerization dips shown

by active vibrations, and quantitative information about the energy, vibrational frequencies and rotational constants of the transition state becomes available. It is especially promising that this analysis stems entirely from a small subset of the vibrational levels; in other words, a full vibrational analysis is not necessary. Special states exist that encode chemically important information, though it may not always be easy to recognize them.

The most exciting outcome of the excellent fits using Eq. 4 is the determination of the transition state energies. The uncertainties in E_{TS} are at least as good as what is currently available from theory. In many cases experiments might only confirm theoretical predictions, but we expect them to sharpen our understanding, and the potential value of our method goes well beyond validating theory. For example, we envision that this approach is a step toward establishing kinetics on the same firm experimental foundation as that already enjoyed by thermochemistry, where precise information is broadly available. This could aid in modeling complex reaction networks as well as provide benchmarks for theoretical calculations.

The next stages in developing the concepts of isomerization dip and effective frequency will require more experimental data for model systems as well as refinement of the basic ideas. For example, it is clear that ω^{eff} is a multi-dimensional quantity, which could be treated by suitable multidimensional analysis. However it is not clear yet how to define $\overline{E}$ in many dimensions. On the experimental side, the MgNC $\leftrightarrow$ MgCN isomerization (*43*) is similar to HCN $\leftrightarrow$ HNC though with a much lower barrier; with higher resolution than has been used so far, it should be possible to get detailed information on the isomerizing levels all the way to the barrier and beyond.

The most promising prospect is the application of this approach to larger molecular systems. For example, the principles presented in this work will provide a framework for experimental characterization of the transition state and detailed mechanism in other reactions, such as *cis-trans* isomerization, as epitomized by stilbene, and 1,2 hydrogen shifts, which are ubiquitous

in organic chemistry. Remarkably little frequency domain spectroscopy has been done at the high energies relevant to chemical kinetics. Partly this is because it was not clear previously what could be learned, and partly it is because the spectra rapidly become very complicated at such energies, so it is difficult to recognize the important patterns. In time it is likely that new classes of experiments will sample the information about isomerization that is encoded in time- or frequency-domain spectra of larger molecules. Our hope is that the concepts and examples described here will be viewed as templates for the characterization of isomerizing systems, thereby challenging and guiding spectroscopists to attack similar problems of chemical interest.

References and Notes

1. S. Arrhenius, *Z. Phys. Chem.* (Akademische Verlagsgesellschaft Geest & Portig, 1889), vol. 2, pp. 226–248.

2. H. Eyring, *J. Chem. Phys.* **3**, 107 (1935).

3. H. Eyring, M. Polanyi, *Z. Phys. Chem. B* **12**, 279 (1931).

4. M. G. Evans, M. Polanyi, *Trans. Faraday Soc.* **31**, 875 (1935).

5. E. Wigner, *Trans. Faraday Soc.* **34**, 29 (1938).

6. D. Townsend, *et al.*, *Science* **306**, 1158 (2004).

7. J. M. Bowman, B. C. Shepler, *Annual Review of Physical Chemistry* **62**, 531 (2011).

8. J. C. Polanyi, A. H. Zewail, *Acc. Chem. Res.* **28**, 119 (1995).

9. R. T. Birge, H. Sponer, *Phys. Rev.* **28**, 259 (1926).

10. R. J. LeRoy, R. B. Bernstein, *J. Chem. Phys.* **52**, 3869 (1970).

11. R. J. Leroy, R. B. Bernstein, *Chem. Phys. Lett.* **5**, 42 (1970).

12. R. N. Dixon, *Trans. Faraday Soc.* **60**, 1363 (1964).

13. The angular momentum quantum number K plays two roles here - that of the asymmetric top rotational quantum number and the linear molecule vibrational angular momentum quantum number, ℓ.

14. M. P. Jacobson, M. S. Child, *J. Chem. Phys.* **114**, 262 (2001).

15. H. Ishikawa, *et al.*, *Annu. Rev. Phys. Chem.* **50**, 443 (1999).

16. S. C. Ross, T. J. Butenhoff, E. A. Rohlfing, C. M. Rohlfing, *J. Chem. Phys.* **100**, 4110 (1994).

17. M. S. Child, *Quantum Monodromy and Molecular Spectroscopy* (John Wiley & Sons, Inc., 2008), vol. 136 of *Adv. Chem. Phys.*, chap. 2, pp. 39–94.

18. S. Yang, V. Tyng, M. E. Kellman, *J. Phys. Chem. A* **107**, 8345 (2003).

19. N. Moiseyev, *Non-Hermitian Quantum Mechanics* (Cambridge University Press, 2011).

20. D. Larese, F. Iachello, *J. Mol. Struct.* **1006**, 611 (2011).

21. M. S. Child, M. P. Jacobson, C. D. Cooper, *J. Phys. Chem. A* **105**, 10791 (2001).

22. N. B. Slater, *Nature* **180**, 1352 (1957).

23. D. W. Oxtoby, S. A. Rice, *J. Chem. Phys.* **65**, 1676 (1976).

24. M. S. Child, *J. Phys. A: Math. Gen.* **31**, 657 (1998).

25. Regarding ω^{eff} vs. $\overline{E}$ as opposed to vs. n: using n simplifies derivations, but $\overline{E}$ is more practical for actual use. Furthermore, plotting against $\overline{E}$ gives more direct information about the PES.

26. G. C. Mellau, *J. Chem. Phys.* **134**, 234303 (2011).

27. T. van Mourik, *et al.*, *J. Chem. Phys.* **115**, 3706 (2001).

28. G. J. Harris, J. Tennyson, B. M. Kaminsky, Y. V. Pavlenko, H. R. A. Jones, *MNRAS* **367**, 400 (2006).

29. J. F. Stanton, C.-M. Huang, P. G. Szalay, *J. Chem. Phys.* **101**, 356 (1994).

30. J. H. Baraban, A. R. Beck, A. H. Steeves, J. F. Stanton, R. W. Field, *J. Chem. Phys.* **134**, 244311 (2011).

31. A. J. Merer, A. H. Steeves, J. H. Baraban, H. A. Bechtel, R. W. Field, *J. Chem. Phys.* **134**, 244310 (2011).

32. J. H. Baraban, *et al.*, *Mol. Phys.* **110**, 2707 (2012).

33. J. H. Baraban, A. J. Merer, J. F. Stanton, R. W. Field, *Mol. Phys.* **110**, 2725 (2012).

34. J. K. G. Watson, M. Herman, J. C. V. Craen, R. Colin, *J. Mol. Spectrosc.* **95**, 101 (1982).

35. A. H. Steeves, A. J. Merer, H. A. Bechtel, A. R. Beck, R. W. Field, *Mol. Phys.* **106**, 1867 (2008).

36. J. D. Tobiason, A. L. Utz, F. F. Crim, *J. Chem. Phys.* **99**, 928 (1993).

37. A. J. Merer, *et al.*, *J. Chem. Phys.* **129**, 054304 (2008).

38. A. H. Steeves, *et al.*, *J. Mol. Spectrosc.* **256**, 256 (2009).

39. In a real system reaction path curvature could occur, such that the normal modes of the minima are not identical to those of the transition state. This would complicate matters, but the modes necessarily evolve smoothly from minimum to transition state.

40. M. Joyeux, S. Y. Grebenshchikov, J. Bredenbeck, R. Schinke, S. C. Farantos, *Adv. Chem. Phys.* **130**, 267 (2005).

41. Z. Bačić, J. C. Light, *J. Chem. Phys.* **86**, 3065 (1987).

42. J. C. Light, Z. Bačić, *J. Chem. Phys.* **87**, 4008 (1987).

43. M. Fukushima, T. Ishiwata, *J. Chem. Phys.* **135**, 124311 (2011).

44. D. Lauvergnat, A. Simon, P. Maître, *Chem. Phys. Lett.* **350**, 345 (2001).

45. A. H. Steeves, Electronic Signatures of Large Amplitude Motions, Ph.D. thesis, Massachusetts Institute of Technology (2009).

46. J. L. Dunham, *Phys. Rev.* **41**, 721 (1932).

47. J. H. Baraban, Spectroscopic Signatures of Isomerization, Ph.D. thesis, Massachusetts Institute of Technology (2013).

48. M. S. Child, R. T. Lawton, *Faraday Discuss. Chem. Soc.* **71**, 273 (1981).

49. M. P. Jacobson, J. P. O'Brien, R. J. Silbey, R. W. Field, *J. Chem. Phys.* **109**, 121 (1998).

50. M. P. Jacobson, R. W. Field, *J. Phys. Chem. A* **104**, 3073 (2000).

51. J. T. Hougen, A. J. Merer, *J. Mol. Spectrosc.* **267**, 200 (2011).

52. P. B. Changala, J. H. Baraban, J. F. Stanton, A. J. Merer, R. W. Field, *J. Chem. Phys.* **140**, 024313 (2014).

53. J. C. Van Craen, M. Herman, R. Colin, J. K. G. Watson, *J. Mol. Spectrosc.* **111**, 185 (1985).

54. A. L. Utz, J. D. Tobiason, E. Carrasquillo M., L. J. Sanders, F. F. Crim, *J. Chem. Phys.* **98**, 2742 (1993).

55. M. Mizoguchi, *et al.*, *J. Phys. Chem. A* **104**, 10212 (2000).

56. P. B. Changala, J. H. Baraban, A. J. Merer, R. W. Field, *Journal of Chemical Physics* **143**, 084310 (2015).

57. G. C. Mellau, *J. Mol. Spectrosc.* **269**, 77 (2011).

58. X. Yang, C. A. Rogaski, A. M. Wodtke, *J. Opt. Soc. Am. B: Opt. Phys.* **7**, 1835 (1990).

59. R. Minyaev, *J. Struct. Chem.* **34**, 829 (1993).

60. C. J. Cerjan, W. H. Miller, *J. Chem. Phys.* **75**, 2800 (1981).

Supplementary Materials

www.sciencemag.org

Figs. S1, S2

Tables S1 to S6

References (45-60)

Figure Captions

Figure 1: Effective frequency plots below their associated model potentials. From left: a) harmonic oscillator, b) Morse oscillator, c) symmetric double minimum potential, and d) asymmetric double minimum potential. In the top panels, the quantized energy levels are marked with dashed lines. In the bottom row, the classical ω^{eff} is shown as a solid line, with the quantum level spacings plotted as open circles vs. $\overline{E}$ (the mid-point energy for each interval). In (c), the upper and lower series of circles correspond to the vibrational level spacings and tunneling splittings, respectively. In (d), the ω^{eff} curve and energy levels for the second minimum are shown in red, and the quantum level spacings are overlaid on the ω^{eff} curves as triangles and squares.

Figure 2: Relationship between potential shape and ω^{eff} illustrated by (a) effective frequency curves and (b) the corresponding potentials as a function of the shape parameter m in Eq. 4.

Figure 3: Salient features of the *cis-trans* isomerization in S_1 C_2H_2. The barrier height and energy difference between the two conformers are shown, as well as the combination of *trans* normal modes (q_3 and q_6) that corresponds to the isomerization coordinate.

Figure 4: The ω_2^{eff} ($\ell = 0$) effective frequency analysis for HCN and HNC. Shown are experimental data points (blue), Dunham-based predictions using only experimental data (green), and the assigned *ab initio* data points (red) (*26*). (See supplementary text for details.) The fitted E_{TS} parameters using Eq. 4 (blue) are compared with the *ab initio* barrier heights (red). A one dimensional cut through the PES is shown as a red dashed line. The unusual shapes of the HNC potential and ω^{eff} plot near 5000 cm^{-1} result from interaction with a low-lying excited diabatic electronic state (*44*).

Figure 5: The ω^{eff} analysis for S_1 C_2H_2. The dip is expected near the *ab initio* value of 4979 cm^{-1}. Data from Tables S1 to S3. (a) Experimental ω^{eff} for the 3^n6^2 levels, shown with fits to Eq. 4. ω_3^{eff} is obtained directly from the progression of 3^n6^2 levels, and ω_6^{eff} is derived from the

$3^n 6^2$ and $3^n 6^1$ levels at a given n_3. (b) Experimental ω_3^{eff} for the $3^n 6^2$ levels as compared to ω_3^{eff} for other progressions with varying quanta of ν_6, shown with fits to Eq. 4. The $3^n 6^2$ series has the sharpest dip, in close analogy to the $K = \ell = 0$ series in the "Dixon dip" (*12*). (c) ω_3^{eff} plots for the 3^n, $3^n 4^2$, and $3^n 6^2$ progressions. The $3^n 4^2$ series follows the normal behavior of the 3^n levels, despite the isomerization dip observed in the $3^n 6^2$ levels. This shows that the torsional mode ν_4 is not involved in the isomerization process at these energies.

Supplementary Materials

Properties of Barrier-Proximal States   In the next two sections we supply reasons why barrier-proximal levels such as the $3^n 6^2$ levels of $\tilde{A}\ ^1A_u$ C_2H_2 deserve special consideration. These characteristics also serve as ways to identify such levels, but are certainly not their only signatures (*45*).

Energetic Considerations   One direct and effective test for identifying barrier-proximal levels is that they do not follow traditional Dunham-type (*46*) effective Hamiltonians. By inverting the usual assignment procedure and ignoring states that fit to conventional models, we can filter for levels that belong to isomerization dip progressions - a counterintuitive method that we applied to great effect in analyzing the HCN/HNC data set. For example, in S_1 C_2H_2 the $3^n 6^2$ levels do not fit well in normal or even extended H^{eff} models, deviating increasingly from their predicted positions along the series (*47*). This fact alone suggests that they belong to a special class of levels with unusual behavior. The idea of local mode behavior is closely related, wherein certain states in polyads with a distinctive energy level pattern exhibit qualitatively new dynamics. Two well-known examples are the stretching overtones in water (*48*), where quanta in the symmetric and antisymmetric stretching normal modes combine to form states with local bond stretching (and eventually bond breaking) character, and the pure bending polyads in S_0 acetylene, where the bending normal modes evolve into "local benders" en route to isomerization to vinylidene (*49, 50*). In those examples, as in our case, the states at the low energy extreme of the polyads fall lower in energy as the polyad number increases, and become isolated. Here, however, our special class of states represents a fundamentally different phenomenon. It is not a result of the polyad-forming interaction, but is rather caused by a separate effect, which might be termed "polyad-breaking". The unequivocal lines of evidence for this distinction are that here the special states *do not* emerge as a function of the polyad quantum number, and also that the

Darling-Dennison parameter K_{4466} varies considerably with v_3, as shown by the rotational fits to the different polyads.
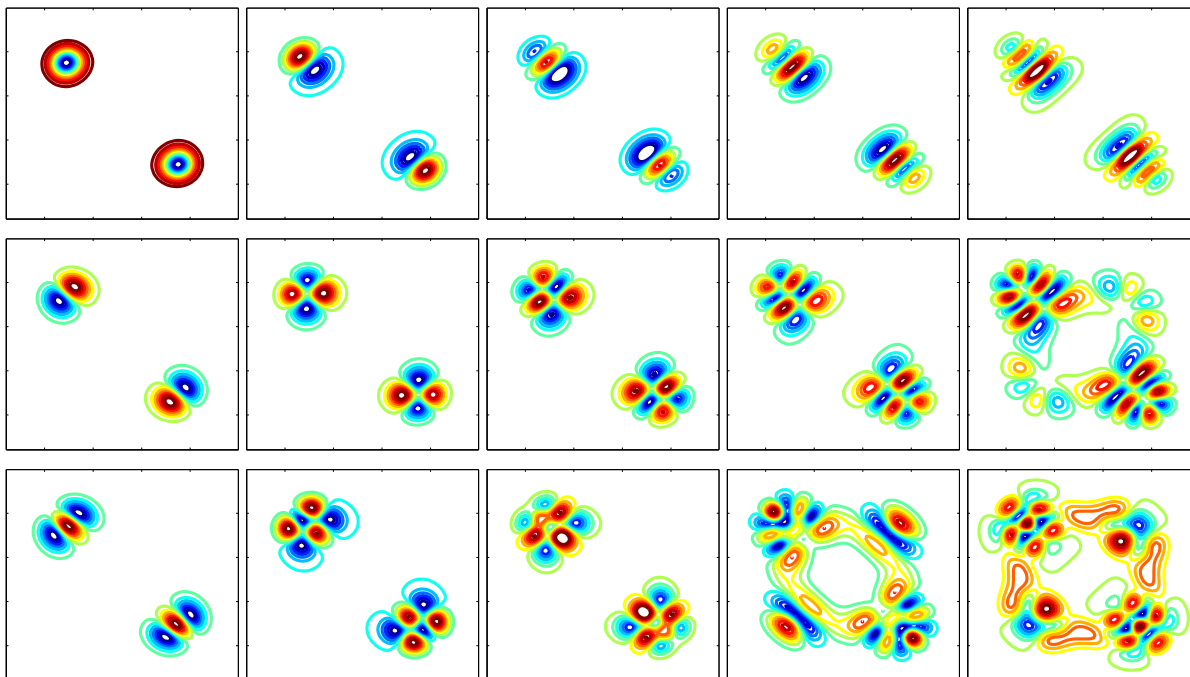

Figure S1: An array of S_1 *trans* C_2H_2 wavefunctions from the calculations in Ref. (*30*), plotted in a two-dimensional ∠CCH plane where the *trans* and *cis* minima exist in the upper left/lower right and lower left/upper right quadrants. The zero point level is shown in the upper left panel, with v_3 increasing to the right, and v_6 increasing down each column. Note the delocalization and nodal pattern distortion that correlates with combined $\{v_3, v_6\}$ excitation.

Wavefunctions A second clue that the 3^n6^2 levels are special can be found by inspecting their wavefunctions. In Fig. S1, *ab initio* wavefunctions from the calculations of Ref. (*30*) are shown for an array of $\{v_3, v_6\}$ states. Most of the functions have the expected nodal structure of two-dimensional harmonic oscillator wavefunctions, with only mild perturbations. Levels with increasing quanta in both ν_3 and ν_6, and especially the 3^n6^2 series shown in the bottom row, however, are delocalized across the *trans* and *cis* minima on the potential surface. The reason is that the 3^n6^2 states are participants in an isomerization dip; they are barrier-proximal, meaning

that their wavefunctions have considerable amplitude directed toward the transition state, and that their energies feel the effect of the strongly anharmonic minimum energy isomerization path.

An important point is that there is clear precedent for variation in the strength of the dip between different progressions of states. In Dixon's original paper (*12*), as mentioned above, the series of levels with K or $\ell = 0$ dipped most strongly, because the states with $K > 0$ must avoid the centrifugal barrier about linearity. Just as the $K = 0$ states in the quasilinear case are singularly effective at accessing the stationary point on the PES because they have no angular momentum, so too in our case the set of barrier proximal $3^n 6^2$ levels is the most effective at reaching toward the isomerization transition state. (See Fig. 5b.) In both cases this access to the stationary point is reflected by the sharpest dip as a function of energy for that specific set of levels.

ω^{eff} **Fits and Input Data** The following tables contain the input term values and fit results for the dip analyses discussed in the main text.

As illustrated in Fig. 1, the quantum level spacings follow the classical ω^{eff} curve closely, except for slight deviations near the stationary point. (See Refs. (*21, 24*).) In the case of S_1 C_2H_2, quantum mechanical tunneling effects appear as K-staggering distortions of the asymmetric top level structure. (*51, 52*) While these perturbations contain valuable information about barrier width, for the purposes of deriving accurate vibrational term values for ω^{eff} analysis, it is necessary to deperturb them. Due to the size of the data set, the HCN/HNC term values have not been deperturbed with respect to tunneling perturbations or anharmonic resonances. Therefore, as described in more detail below, some data points at high $\overline{E}$ were excluded from the fits, in addition to the points that are missing due to the energy cutoff of the *ab initio* eigenenergies. Listed below in Table S3 are additional observed rotational transitions necessary to obtain the

3

term values in Table S2.

Table S1: ω^{eff} Fits to $3^n 6^m$ Levels of S_1 *trans* C_2H_2. All parameters in cm^{-1}, except m, which is dimensionless. Uncertainties are 2σ. The ω_6^{eff} data sets are constructed by taking the average and difference of the energies of the $3^n 6^m$ series listed and the $3^n 6^{m-1}$ levels.

Fit	ω_0	E_{TS}	m	RMS
$\omega_3^{\mathrm{eff}} : 3^n$	1058 ± 21	$2\mathrm{e}4 \pm 2\mathrm{e}5^*$	2.3 ± 19	3.4
$\omega_3^{\mathrm{eff}} : 3^n 6^1$	1039 ± 13	4845 ± 591	14.3 ± 6	0.65
$\omega_3^{\mathrm{eff}} : 3^n 6^2$	1030 ± 30	4692 ± 33	11.5 ± 3	1.5
$\omega_6^{\mathrm{eff}} : 3^n 6^1$	777.6 ± 2	5074 ± 83	6.3 ± 0.3	0.48
$\omega_6^{\mathrm{eff}} : 3^n 6^2$	796.6 ± 4	4846 ± 4	6.3 ± 0.2	0.90

*Note that for the $\omega_3^{\mathrm{eff}} : 3^n$ fit the E_{TS} value is not meaningful, since m should be fixed at 2 for this Morse-like series.

S_1 C_2H_2 Effective Frequency Analysis The fitted parameters confirm the expectations laid out earlier. The barrier height obtained by adding $\omega_6/2$ (for reasons explained below in the section on Zero Point Energy) to the 4692 cm^{-1} value for E_{TS} is 5091 cm^{-1}; this differs from the *ab initio* value of 4979 cm^{-1} by only 2%, well within the *ab initio* uncertainty of a few hundred wavenumbers. The ω_0 values are in line with the experimentally known harmonic frequencies and anharmonicities, and the m values fall in a range that seems sensible based on Fig. 2.

HCN/HNC Effective Frequency Analysis Two different types of data were used for the HCN/HNC ω^{eff} analysis. The first data set is the product of assigning the eigenenergies (*26*) generated by a high level variational *ab initio* calculation (*27, 28*), up to and above the isomerization barrier, to a maximum energy of 18000 cm^{-1}. The second data set consists of experimental eigenenergies up to 10000 cm^{-1} from HOTGAME (Hot Gas Molecular Emission) experiments of one of the authors (*26, 57*). Based on these term values (and those of 14 states from Ref. (*58*)), Dunham-type effective Hamiltonians have been determined for HCN and HNC.

4

Table S2: Term Values Used in the S_1 C_2H_2 ω^{eff} Fits. All energies in cm^{-1}. T_0 and $J=K=0$ values used where available. See Ref. (*30*).

v_3 \ v_6	0	1	2
0	0	768.26‡	1531.02$^\#$
1	1047.55*	1785.53§	2511.39**
2	2077.71*	2778.76§	3456.38**
3	3088.14*	3739.98$^\|$	4339¶
4	4072.95*	4642.93¶	4993.78¶
5	5042.78†		

*From Refs. (*34, 53*)

†From Ref. (*53*), but with a K-staggering of $+6.31$ cm^{-1} removed.

‡From Ref. (*54*)

§From Ref. (*55*).

$^\|$From Ref. (*33*).

¶The term value for 3^46^1 is based on our IR-UV spectra, with a very large K-staggering of $+27.63$ cm^{-1} removed. The term value for 3^36^2 is based on a $K = 1$ level observed at 46547 cm^{-1}, with an estimated effective $A - \overline{B}$ of 8 cm^{-1}. The term value for 3^46^2 combines corrected data from Ref. (*53*) with our H atom action spectra (*56*); also, a K-staggering of -6.89 cm^{-1} has been removed.

$^\#$From Ref. (*37*).

**From Ref. (*38*).

Table S3: (a) Assigned lines of the 46656 cm^{-1} $\Delta - \Pi$ subband of $3^4 6^2$, observed in H atom action spectra (56). Values in cm^{-1}.

		$K = 2 - 1$	
J	R	Q	P
1	46660.93		
2	46662.84	46656.22	
3	46664.65	46655.84	46649.19
4	46668.18	46655.16	

(b) Assigned lines of the 46547 cm^{-1} $K' = 1 - 0$ subband of $3^3 6^2$. Values in cm^{-1}. Blended lines marked with *.

		$K = 1 - 0$	
J	R	Q	P
1	46550.93	46546.60	
2	46553.23	46546.09	
3	46554.82	46545.13	46539.20
4			46536.75
5			46533.65*

(c) $3^4 6^1$ $K = 0 - 2$ sublevels.

K'	T_0			B			$10^2 q$			r.m.s.
0	46826.68	$\pm$	0.028	1.0628	$\pm$	0.0010				0.018
1	46867.29		0.026	1.0433		0.0019	4.16	$\pm$	0.23	0.015
2	46878.59		0.089	1.0555		0.0064	-0.033		0.030	0.030

The $K = 1 - 0$ interval minus $(K = 2 - 0)/4$ gives a K-staggering of 28 cm^{-1}. The usual Coriolis interactions in B^1 polyads are rendered negligible for our purpose here by the large $\nu_3 - \nu_6$ anharmonicity. q is the coefficient of $[J(J+1)]^K$, with a positive value if the e levels are above the f in energy.

Using these effective Hamiltonians, the vibrational eigenenergies and ω_2^{eff} for both isomers have been predicted up to the isomerization barrier. For HCN there is remarkable agreement with the *ab initio* data set; the divergence of the predictions from the *ab initio* data for HNC will be explained below. In the case of HCN, there are two reasons why the predicted effective frequencies match the calculated ω^{eff} derived from *ab initio* data. First, the ℓ-dependence of states in the effective Hamiltonian is very accurately described, due to the large number of ℓ-subbands detected in the emission spectra (up to $v_2 = 15$ for $\ell > 0$ states). Second, the differences between the *ab initio* and predicted eigenenergies increase with bending excitation, but these errors are partially compensated when calculating the effective frequency.

The generally excellent correspondence between the *ab initio* data set and the experimental measurements gives us confidence that the spectroscopically assigned *ab initio* eigenenergies are an appropriate tool for examining the dynamics of the [H,C,N] system. Consequently, we have utilized this information to conduct the HCN and HNC ω^{eff} analyses.

As mentioned above, for HNC the effective Hamiltonian ω^{eff} does not follow the *ab initio* ω^{eff} (Fig. 4) because of interaction with a low-lying diabatic excited electronic state (*44*). To compensate for the unusual form of the potential, an *ad hoc* Gaussian term has been added to Eq. 4 for the HNC fits, and this issue does not appear to cause any major difficulties.

Table S5 lists the parameters of Eq. 4 determined in the effective frequency analysis for HCN and HNC. In some cases, states are excluded due to perturbations or because they lie above the maximum energy of the *ab initio* data set; progressions with high vibrational angular momentum or multiple stretch excitations extend to higher energies and often exceed the 18000 cm^{-1} limit. For these fits the ω^{eff} analysis is approximate, and based mainly on estimates of the m parameter, which is then kept fixed. The ω_0 parameter has been divided by two in the HCN/HNC fits to correspond with the bending frequency.

Table S4: Saddle point energies determined from the $\ell = 0$ effective frequency fit analyses. ΔV_{1D} are the barrier heights of the 1-dimensional effective bending potentials (*40*). Uncertainties given in parentheses are 1σ.

Fit	HCN			HNC		
	E_{TS}	ΔV_{1D}	$E_{TS} - \Delta V_{1D}$	E_{TS}	ΔV_{1D}	$E_{TS} - \Delta V_{1D}$
$0v_20$	16695(17)	16344*	2.1%	11533(124)	10924*	5.6%
$1v_20$	15872(21)	15597	1.7%	9950(215)	9811	1.4%
$0v_21$	16220(1)	16241	0.1%	11542(270)	10881	6.1%

*The bare *ab initio* barrier heights are 16798 and 11517 cm^{-1} for HCN and HNC, respectively. The fitted E_{TS} values agree to within 1%.

Table S5: Fitted E_{TS}, m and ω_0 parameters for the HCN and HNC effective frequency analysis. Uncertainties in parentheses are 1σ, and values in brackets were fixed. Data from Table S6.

| Fit $v_1 v_2 v_3,\ \ell$	E_{TS} HCN	m HCN	ω_0 HCN	E_{TS} HNC	m HNC	ω_0 HNC
$0v_20, \ell = 0$	16695(17)	8.8(2)	712(1)	11533(124)	[6.4]	474(3)
$0v_20, \ell = 1$	16764(1)	8.8(2)	710(2)			
$0v_20, \ell = 2$	16577(7)	9.0(1)	710(1)			
$0v_20, \ell = 3$	16743(75)	8.7(3)	711(2)			
$0v_20, \ell = 4$	16530(3)	9.3(1)	710(1)			
$0v_20, \ell = 5$	16683(37)	9.0(2)	712(1)			
$0v_20, \ell = 6$	17217(74)	8.4(2)	715(1)			
$0v_20, \ell = 7$	17146(187)	8.6(4)	716(2)			
$0v_20, \ell = 8$	17400(142)	8.4(3)	718(2)			
$0v_20, \ell = 9$	17605(88)	[8.6]	717(1)			
$0v_20, \ell = 10$	17640(59)	8.5(3)	720(3)			
$0v_20, \ell = 11$	18046(158)	[8.6]	718(2)			
$0v_20, \ell = 12$	18039(58)	[8.6]	721(2)			
$0v_21, \ell = 0$	16220(1)	9.8(4)	706(4)	11542(270)	[6.4]	470(4)
$1v_20, \ell = 0$	15872(21)	7.6(3)	699(4)	9950(215)	[4.9]	[474]

8
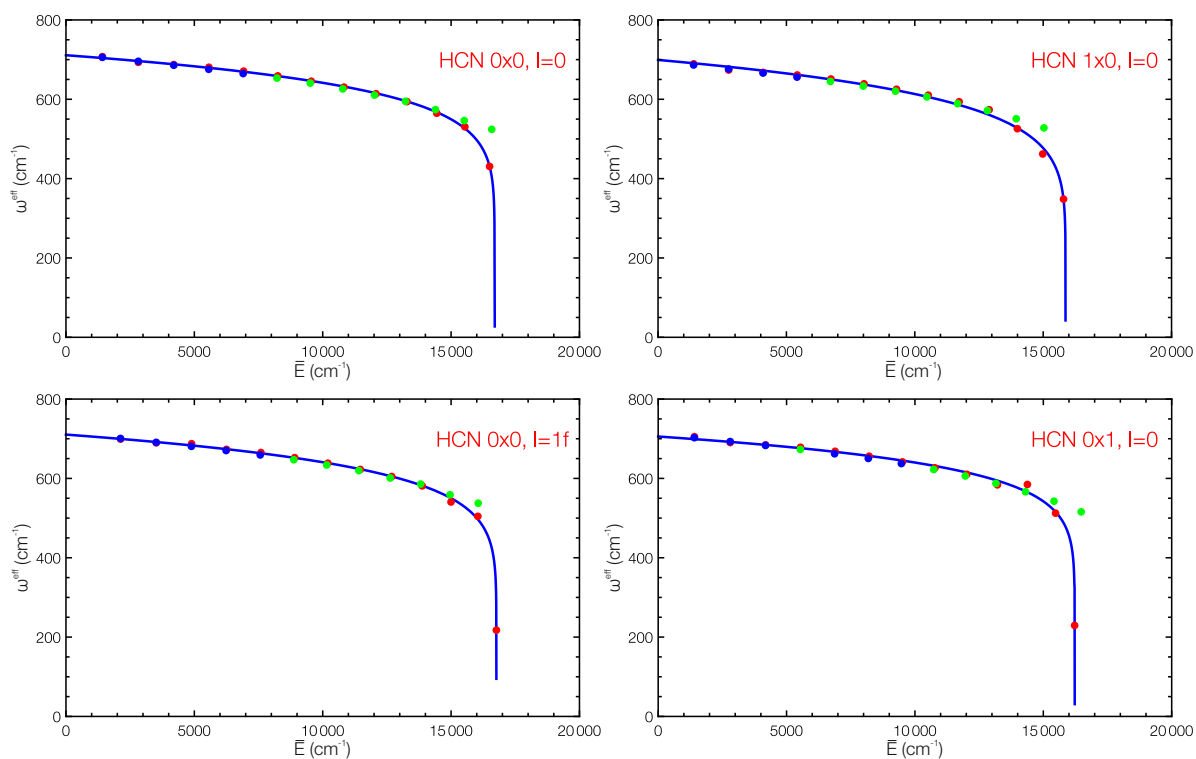
Figure S2: Representative isomerization dip plots for HCN. As in Fig. 4, shown are experimental data points (blue), Dunham-based predictions using only experimental data (green), and the assigned *ab initio* data points (red). (*26*)

Zero-Point Energy Our model effective frequency expression, $\omega^{\text{eff}} = \omega_0(1 - E/E_{TS})^{1/m}$, is explicitly a function of E, the absolute vibrational energy referenced to the minimum of the effective 1D potential. ($\overline{E}$, obtained by averaging adjacent quantized eigenergies, is locally approximately equal to E.) Spectroscopic measurements, however, provide only the relative vibrational energy referenced to the zero-point energy of the potential, E_0, such that $E = E_0 + G$, where G is the relative vibrational energy. It would be convenient to find an algebraic expression for E_0, in order to use the measured G values directly in the expression for ω^{eff}. Applying the method of semiclassical quantization, we can determine such an expression for E_0 in terms of ω_0, E_{TS}, and m that is self-consistent with our effective frequency ansatz Eq. 4.

We begin with the basic relation between the periodic frequency of 1D motion as a function of energy, $\omega(E)$, and the classical action, J, of that periodic orbit

$$\frac{1}{\omega(E)} = \frac{\partial J}{\partial E}. \tag{S1}$$

Applying WKB quantization to the classical action, we have the following integral relation for the zero-point energy, E_0,

$$\int_0^{E_0} dE \frac{1}{\omega(E)} = \int_0^{E_0} dE \frac{\partial J}{\partial E}$$
$$= J(E_0)$$
$$\overset{!}{=} \frac{1}{2} \tag{S2}$$

(We have fixed the minimum of the potential at $V = 0$, such that $J(E = 0) = 0$.)

We now substitute our ω^{eff} expression into the integrand and evaluate the integral:

$$\int_0^{E_0} dE \frac{1}{\omega^{\text{eff}}} = \int_0^{E_0} dE \frac{1}{\omega_0}\left(1 - \frac{E}{E_{TS}}\right)^{-1/m} = \frac{1}{2} \tag{S3}$$
$$\Rightarrow \frac{1}{2} = \frac{1}{\omega_0}\frac{m}{m-1}\left(E_{TS} + (E_0 - E_{TS})(1 - E_0/E_{TS})^{-1/m}\right) \tag{S4}$$

Eq. S4 can be solved for E_0, yielding

$$E_0 = E_{TS} \left(1 - \left[1 - \frac{\omega_0}{2E_{TS}} \left(1 - \frac{1}{m} \right) \right]^{\frac{m}{m-1}} \right) \quad \text{(S5)}$$

In Eq. S5, we have an expression for E_0 in terms of the other model parameters that is self-consistent with the ω^{eff} model under semiclassical quantization.

This expression conforms to the expected limiting cases. For a harmonic oscillator ($m \to \infty$), the expression becomes independent of m and E_{TS}, giving

$$E_0|_{m \to \infty} = \frac{\omega_0}{2} \quad \text{(S6)}$$

For a Morse oscillator ($m = 2$), the evaluation is simple and yields

$$E_0|_{m=2} = \frac{\omega_0}{2} - \frac{\omega_0^2}{16E_{TS}}, \quad \text{(S7)}$$

which is the exact Morse result if E_{TS} is identified with D_e.

The derivation above applies principally to one-dimensional cases, since otherwise the zero-point energy is not separable into components parallel and perpendicular to the reaction coordinate. Accordingly, in such cases we set the zero of energy at that of the vibrationless level for fitting purposes. This implies that the fitted E_{TS} excludes the zero point energy of the effective isomerization path. (See Table S1 and the surrounding discussion.) The zero point energy of the lowest frequency mode that participates in the isomerization is a good approximation to this quantity, because the minimum energy isomerization path is always parallel to that mode at the potential minimum. (*59, 60*)

The Meaning of m   The effective frequency dip model given by Eq. 4 contains three independent parameters, ω_0, E_{TS}, and m. The first two in this set have simple relations to the shape of the potential energy surface: ω^{eff} describes the curvature near the potential minimum and E_{TS} the transition state energy or barrier height.

In this section, we show how the parameter m, originally introduced as an empirical shape parameter (Fig. 2), can also be directly identified with a simple physical characteristic of the potential surface. We begin with the standard Rydberg-Klein-Rees (RKR) inversion expression

$$r_+(v) - r_-(v) = 2\sqrt{\frac{\hbar^2}{2\mu}} \int_{-1/2}^{v} \frac{1}{\sqrt{G(v) - G(u)}} du \tag{S8}$$

where r_+ (r_-) is the outer (inner) classical turning point of the 1D potential, μ is the effective mass, v and u are vibrational quantum numbers (treated as continuous), and $G(v)$ is the vibrational energy as a function of v with $G(v = -\frac{1}{2}) = 0$. It is convenient to change variables in Eq. S8 from quantum numbers to vibrational energies. Letting $G(u) = \epsilon$ and $G(v) = E$ yields

$$r_+(E) - r_-(E) = 2\sqrt{\frac{\hbar^2}{2\mu}} \int_0^E \frac{1}{\omega^{\text{eff}}(\epsilon)} \frac{1}{\sqrt{E - \epsilon}} d\epsilon \tag{S9}$$

where we have used the definition of $\omega^{\text{eff}}(\epsilon) \equiv \partial G(u)/\partial u$. Inserting our expression for $\omega^{\text{eff}}(\epsilon)$ (Eq. 4) and defining the mass-weighted distance between turning points $\Delta(E) \equiv \sqrt{\mu}[r_+(E) - r_-(E)]$ we have

$$\Delta(E) = \sqrt{2\hbar^2} \int_0^E \frac{1}{\omega_0(1 - \epsilon/E_{TS})^{1/m}} \frac{1}{\sqrt{E - \epsilon}} d\epsilon \tag{S10}$$

We now perform another change of variables to isolate the dimensioned quantities. Letting $x = \epsilon/E_{TS}$ and $X = E/E_{TS}$, we obtain

$$\Delta(E) = \frac{\sqrt{2\hbar^2 E_{TS}}}{\omega_0} \int_0^{X=E/E_{TS}} \frac{1}{(1 - x)^{1/m}} \frac{1}{(X - x)^{1/2}} dx. \tag{S11}$$

The dimensionless integral in Eq. S11 can be expressed relatively succinctly in terms of the $_2F_1$ hypergeometric functions. However, this general result is not particularly useful. To determine the significance of the parameter m, we evaluate Eq. S11 at $E = E_{TS}$ (i.e. $X = 1$):

$$\Delta(E = E_{TS}) = \frac{\sqrt{2\hbar^2 E_{TS}}}{\omega_0} \int_0^1 \frac{1}{(1 - x)^{\frac{1}{m} + \frac{1}{2}}} dx \tag{S12}$$

$$= \frac{\sqrt{2\hbar^2 E_{TS}}}{\omega_0} \left[\frac{(1 - x)^{-\frac{1}{m} + \frac{1}{2}}}{\frac{1}{m} - \frac{1}{2}} \right]_0^1 \tag{S13}$$

12

$$= \frac{\sqrt{2\hbar^2 E_{TS}}}{\omega_0} \frac{1}{\frac{1}{2} - \frac{1}{m}}. \tag{S14}$$

This expression relates $\Delta(E = E_{TS})$, the mass-weighted distance between the classical turning points at the energy of the barrier E_{TS}, directly to m. Alternatively, for a given E_{TS}, changing m varies the steepness of the ascent to the saddle point. In the limits $m \to 2$ and $m \to \infty$, we have $\Delta \to \infty$ and $\Delta \to 2\sqrt{2E_{TS}}/(\omega_0/\hbar)$, the expected results for a Morse oscillator and harmonic oscillator, respectively. In the case of HCN, where the isomerization path is symmetric about $\theta \leftrightarrow -\theta$, $\Delta(E = E_{TS})$ equals the distance between two symmetry-equivalent transition state barriers and thus is twice the distance between the transition state barrier and the potential minimum. In this way, we can analytically relate m to the isomerization path distance, which in addition to ω_0 and E_{TS}, is another chemically relevant characteristic of the potential energy surface.